preparation of alcohols bearing adjacent tri- and tetrasubstituted stereogenic centers. We anticipate that the design of optimal ligand scaffolds will enable the transformation of a broader range of unactivated olefins, ultimately delivering a powerful tool for the asymmetric addition of olefin-derived nucleophiles to carbonyls that will be of broad synthetic utility.

REFERENCES AND NOTES

1. E. J. Corey, L. Kürti, *Enantioselective Chemical Synthesis: Methods, Logic and Practice* (Direct Book Publishing, 2010).
2. P. Knochel *et al.*, *Angew. Chem. Int. Ed.* **42**, 4302–4320 (2003).
3. R. Noyori, M. Kitamura, *Angew. Chem. Int. Ed. Engl.* **30**, 49–69 (1991).
4. L. Pu, H.-B. Yu, *Chem. Rev.* **101**, 757–824 (2001).
5. J. L. Stymiest, V. Bagutski, R. M. French, V. K. Aggarwal, *Nature* **456**, 778–782 (2008).
6. O. Riant, J. Hannedouche, *Org. Biomol. Chem.* **5**, 873–888 (2007).
7. M. Shibasaki, M. Kanai, *Chem. Rev.* **108**, 2853–2873 (2008).
8. H.-Y. Jang, M. J. Krische, *Acc. Chem. Res.* **37**, 653–661 (2004).
9. E. Skucas, M.-Y. Ngai, V. Komanduri, M. J. Krische, *Acc. Chem. Res.* **40**, 1394–1401 (2007).
10. I. P. Bower, I. S. Kim, R. L. Patman, M. J. Krische, *Angew. Chem. Int. Ed.* **48**, 34–46 (2009).
11. M. R. Chaulagain, G. J. Sormunen, J. Montgomery, *J. Am. Chem. Soc.* **129**, 9568–9569 (2007).
12. E. P. Jackson *et al.*, *Acc. Chem. Res.* **48**, 1736–1745 (2015).
13. K. M. Miller, W.-S. Huang, T. F. Jamison, *J. Am. Chem. Soc.* **125**, 3442–3443 (2004).
14. R. M. Moslin, K. Miller-Moslin, T. F. Jamison, *Chem. Commun.* **2007**, 4441–4449 (2007).
15. F. Meng, F. Haeffner, A. H. Hoveyda, *J. Am. Chem. Soc.* **136**, 11304–11307 (2014).
16. F. Meng, H. Jang, B. Jung, A. H. Hoveyda, *Angew. Chem. Int. Ed.* **52**, 5046–5051 (2013).
17. A. M. Berman, J. S. Johnson, *J. Am. Chem. Soc.* **126**, 5680–5681 (2004).
18. M. T. Pirnot, Y.-M. Wang, S. L. Buchwald, *Angew. Chem. Int. Ed.* **55**, 48–57 (2016).
19. Y. Mikki, K. Hirano, T. Satoh, M. Miura, *Angew. Chem. Int. Ed.* **52**, 10830–10834 (2013).
20. Y. Mikki, K. Hirano, T. Satoh, M. Miura, *Org. Lett.* **16**, 1498–1501 (2014).
21. D. Nishikawa, K. Hirano, M. Miura, *J. Am. Chem. Soc.* **137**, 15620–15623 (2015).
22. Y. Xi, T. W. Butcher, J. Zhang, J. F. Hartwig, *Angew. Chem. Int. Ed.* **55**, 776–780 (2016).
23. J. Deschamp, O. Chuzel, J. Hannedouche, O. Riant, *Angew. Chem. Int. Ed.* **45**, 1292–1297 (2006).
24. D. Zhao, K. Oisaki, M. Kanai, M. Shibasaki, *J. Am. Chem. Soc.* **128**, 14440–14441 (2006).
25. B. H. Lipshutz, B. Amorelli, J. B. Unger, *J. Am. Chem. Soc.* **130**, 14378–14379 (2008).
26. A. Saxena, B. Choi, H. W. Lam, *J. Am. Chem. Soc.* **134**, 8428–8431 (2012).
27. B. H. Lipshutz, K. Noson, W. Chrisman, A. Lower, *J. Am. Chem. Soc.* **125**, 8779–8789 (2003).
28. L. M. Geary, S. K. Woo, J. C. Leung, M. J. Krische, *Angew. Chem. Int. Ed.* **51**, 2972–2976 (2012).
29. V. Komanduri, M. J. Krische, *J. Am. Chem. Soc.* **128**, 16448–16449 (2006).
30. Y. Sasaki, Y. Horita, C. Zhong, M. Sawamura, H. Ito, *Angew. Chem. Int. Ed.* **50**, 2778–2782 (2011).
31. C.-H. Ding, X.-L. Hou, *Chem. Rev.* **111**, 1914–1937 (2011).
32. S.-L. Shi, L.-W. Xu, K. Oisaki, M. Kanai, M. Shibasaki, *J. Am. Chem. Soc.* **132**, 6638–6639 (2010).
33. K. R. Fandrick *et al.*, *J. Am. Chem. Soc.* **133**, 10332–10335 (2011).
34. E. Ascic, S. L. Buchwald, *J. Am. Chem. Soc.* **137**, 4666–4669 (2015).
35. A. M. Whittaker, G. Lalic, *Org. Lett.* **15**, 1112–1115 (2013).
36. J. Clayden, P. Maclellan, *Beilstein J. Org. Chem.* **7**, 582–595 (2011).

CATALYSIS

Thermally stable single-atom platinum-on-ceria catalysts via atom trapping

John Jones,[1]* Haifeng Xiong,[1]* Andrew T. DeLaRiva,[1] Eric J. Peterson,[1] Hien Pham,[1] Sivakumar R. Challa,[1] Gongshin Qi,[2] Se Oh,[2] Michelle H. Wiebenga,[2] Xavier Isidro Pereira Hernández,[3] Yong Wang,[3,4] Abhaya K. Datye[1]†

Catalysts based on single atoms of scarce precious metals can lead to more efficient use through enhanced reactivity and selectivity. However, single atoms on catalyst supports can be mobile and aggregate into nanoparticles when heated at elevated temperatures. High temperatures are detrimental to catalyst performance unless these mobile atoms can be trapped. We used ceria powders having similar surface areas but different exposed surface facets. When mixed with a platinum/aluminum oxide catalyst and aged in air at 800°C, the platinum transferred to the ceria and was trapped. Polyhedral ceria and nanorods were more effective than ceria cubes at anchoring the platinum. Performing synthesis at high temperatures ensures that only the most stable binding sites are occupied, yielding a sinter-resistant, atomically dispersed catalyst.

Diesel oxidation catalysts (DOCs) are used in the automotive industry to oxidize harmful emissions that contain CO, NO, and hydrocarbons. Pt is very active for such oxidation reactions (*1*, *2*). Under oxidizing conditions at high temperatures, the Pt nanoparticles on the oxide support sinter to form large particles, which leads to a loss of surface area and hence decreased catalytic activity, so there is commercial interest in developing sinter-resistant catalysts that can maintain activity over long-term operation. We previously found that the mechanism of activity loss involves the emission of mobile species from small particles and their capture by large particles—a process called Ostwald ripening (*3*, *4*). Here, we show that the conditions under which nanoparticles emit mobile species are also ideally suited to generating atomically dispersed catalysts if the mobile species can be effectively trapped. Platinum group metals can be trapped in ionic form in complex oxides (*5*), but they can be lost inside the bulk oxide, where they are no longer effective as a catalyst. An ideal support for trapping metal species is one in which the mobile species stay at the surface so that they retain catalytic activity.

Our studies were performed at 800°C in oxidizing ambient conditions typically used for accelerated testing of DOCs. Under these conditions, Pt can be emitted as volatile PtO_2 (*6*) which can lead to transport of Pt from the DOC catalyst to the downstream selective catalytic reduction (SCR) catalyst (*7*). A vapor-phase approach for the synthesis of catalysts—specifically, transferring Pt from a metal foil to alumina—was reported previously (*8*), but the ability of supports such as ceria to trap atomically dispersed Pt was not recognized. In industry, the vapor-phase transport of metal oxides is regarded as a leading cause of catalyst degradation (*9*). Thus, we set out to find materials that could effectively trap the mobile species. In previous work, we found that PdO was able to trap mobile PtO_2, forming metallic Pt-Pd particles (*10*). The remarkable efficiency of PdO for trapping Pt suggests that other oxides could play a similar role. McVicker *et al.* (*11*) had implied that CaO, SrO, and BaO may slow the rates of Ir sintering through the presence of acid sites on the support.

We worked with ceria as a support because Ce-Zr-Y was shown by Nagai *et al.* (*12*) to be effective for inhibiting the sintering of Pt by

[1]Department of Chemical and Biological Engineering and Center for Micro-Engineered Materials, University of New Mexico, Albuquerque, NM 87131, USA. [2]General Motors Global R&D, 30500 Mound Road, Warren, MI 48090, USA. [3]Voiland School of Chemical Engineering and Bioengineering, Washington State University, Pullman, WA 99164, USA. [4]Institute for Integrated Catalysis, Pacific Northwest National Laboratory, Richland, WA 99354, USA.
*These authors contributed equally to this work. †Corresponding author. Email: datye@unm.edu

forming a surface complex. The ability of ceria to improve the sinter resistance of metals in automotive catalysts has been explained in terms of lowering the surface energy of nanoparticles (enhanced wetting) (13). However, as we show here, an additional benefit is the ability of ceria to trap Pt in an atomically dispersed state. Other catalyst supports have been shown to stabilize Pt in the form of isolated atoms—for example, penta-coordinated Al^{3+} sites on alumina (14), FeO_x (15), and the (111) surface of $MgAl_2O_4$ (16). However, when these catalysts are aged at 800°C in air (16, 17), the formation of large crystalline Pt particles can be detected via x-ray diffraction (XRD). The complete absence of an XRD peak for Pt demonstrates that the sample contains only atomically dispersed species, which can be confirmed by reactivity measurements, energy-dispersive spectroscopy (EDS), aberration-corrected scanning transmission electron microscopy (AC-STEM), and diffuse reflectance infrared Fourier transform spectroscopy (DRIFTS).

Exposing ceria powders with different surface facets allowed us to determine the most effective surface for trapping Pt. Ceria can be synthesized in well-defined shapes, specifically nanorods, cubes, and octahedra (18). The similar specific reactivity of octahedra and nanorods for the water-gas shift reaction (19) suggests that the rods expose dominant (111) facets, contrary to the previously reported morphology of the nanorods (18). Ceria nanoshapes have been studied for their role in Pt sintering and redispersion (20). Density functional theory (DFT) calculations by Bruix et al. (21) suggested that CeO_2 (100) surfaces provide the right geometry to stabilize Pt^{2+} by bonding to O^{2-} in square pockets. Neitzel et al. (22) showed that the Pt cations are stable on the surface rather than diffusing into the ceria bulk. However, the highest temperature achieved in

these previous studies was much lower than the aging temperature of DOCs (21).

We sought to determine the effectiveness of various ceria surface facets for trapping Pt at typical DOC aging conditions, 800°C in air. We introduced ceria powders as a separate phase by simple physical mixing. Three different ceria shapes were used: cubes (50 m²/g), nanorods (90 m²/g), and what we refer to as polyhedral ceria (89 m²/g). The latter, obtained by calcination of cerium nitrate, consists of nanoparticles of truncated octahedra, which expose (111) surface facets, because they constitute the most stable low-index surface of ceria (23). The rounded nature of these polyhedral particles indicates that other less prominent surfaces, as well as step edges, must also be exposed (figs. S1 and S2).

The STEM image of the as-prepared Pt/La-Al_2O_3 catalyst, nominally 1 weight percent (wt %) (Fig. 1A), shows small Pt particles on the alumina support. After the sample was aged at 800°C for 10 hours in flowing air, large Pt crystallites were formed (Fig. 1B). After aging, EDS analysis in a scanning electron microscope (SEM) showed ~0.8 wt % Pt (table S1), which was confirmed via XRD analysis (24). XRD patterns corroborated the rapid sintering, as evident from the well-defined, sharp reflections for face-centered cubic (fcc) Pt in Fig. 1C; the broad reflections and the background in this pattern come from the alumina support.

The as-prepared 1 wt % Pt/La-Al_2O_3 catalyst was physically mixed with ceria powders in a weight ratio of 2:1 (33 wt % ceria) and then subjected to aging in flowing air. TEM/STEM images of the physical mixtures after aging show that the Al_2O_3 and CeO_2 phases in the mixture are attached to each other (fig. S3). Furthermore, the STEM image revealed that no Pt was present on the alumina because it had migrated to the CeO_2

phase (figs. S3 and S4) and was trapped, forming subnanometer Pt species. XRD patterns of the physically mixed catalysts after aging at 800°C for 10 hours in air are shown in Fig. 1D, curves a to c. The size of the Pt(111) peak gets smaller in samples a to c, suggesting improved efficiency for trapping Pt (decrease in the amount of the crystalline Pt phase). The sample aged for 1 week in air (Fig. 1D, curve d) shows no Pt peak at all, indicating the complete absence of large Pt particles. Because ceria can scatter x-rays, it causes a decrease in the size of Pt peak. This effect of ceria is seen by comparing the XRD pattern of the aged Pt/La-Al_2O_3 (Fig. 1C) with the XRD pattern of the same sample after mixing with ceria (2 parts Pt/La-Al_2O_3:1 part ceria) (Fig. 1D, curve e).

The inset in Fig. 1D shows magnified views of the Pt(111) reflection. The size and sharpness of this peak are indicative of the crystallite size of Pt. The splitting of the peak into a doublet, the $K_{\alpha 1}$ and $K_{\alpha 2}$, is further evidence of large Pt crystallites. With such large particles, XRD cannot be used to estimate crystallite dimensions because size-induced broadening is smaller than the instrumental broadening. The size of the Pt peak gives us a visual indication of the amount of crystalline Pt in these samples. The Rietveld refinement method (fig. S5) was used to quantify the amount of crystalline Pt visible to XRD, which is reported for each of these samples in table S2. The calculated value of 0.81 wt % Pt in the reference sample (Fig. 1D, curve e) agrees with independent EDS analysis of the overall composition of this sample (table S1). The excellent agreement between XRD-derived composition and elemental analysis allows us to estimate the amount of crystalline Pt visible to XRD in each of these samples. Subtracting the amount of crystalline Pt from the total Pt gives us the amount of atomically dispersed Pt in each sample (table S2).
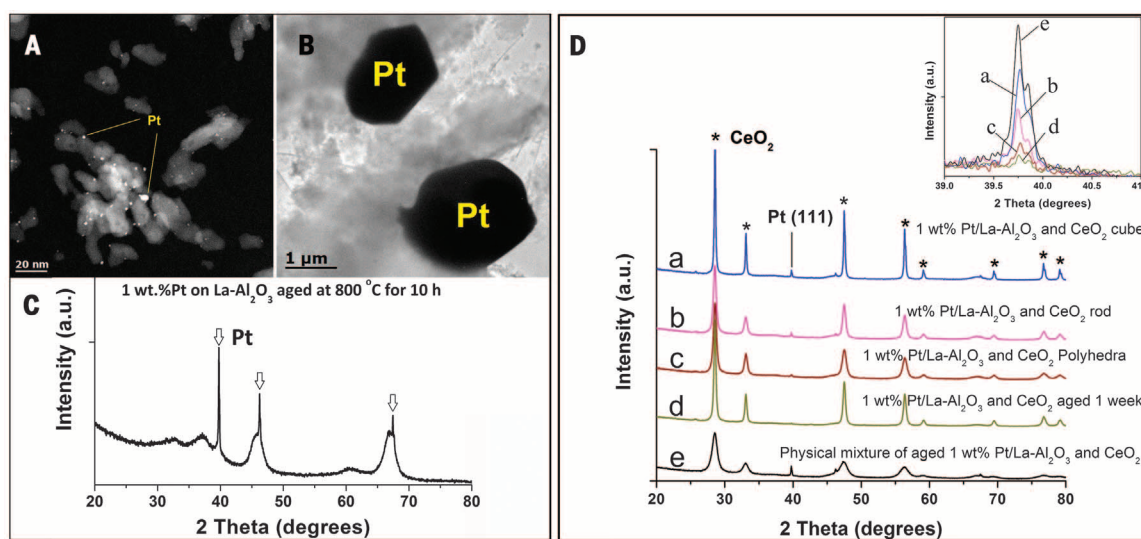
Fig. 1. The transfer of Pt from alumina to ceria leads to a decrease in size of the Pt(111) XRD peak. (**A**) HAADF STEM image of 1 wt % Pt/La-Al_2O_3 after calcination in air at 350°C for 5 hours. (**B**) TEM image of this catalyst after aging at 800°C in air for 10 hours. (**C**) XRD pattern of this catalyst after aging in air at 800°C for 10 hours. The sharp Pt reflections (vertical arrows) arise from the large particles seen in the TEM image (B), whereas the broad peaks come from the alumina support. (**D**) XRD patterns of physical mixtures of 1 wt % Pt/La-Al_2O_3 and ceria powders (weight ratio 2:1) after aging at 800°C for 10 hours in flowing air [(a) to (c)], aged for 1 week with polyhedral ceria (d), and a reference sample (e) where the Pt/La-alumina catalyst was first aged as in (C), then mixed with polyhedral ceria in the same weight ratio. The asterisks show the CeO_2 reflections whose peak widths vary as a result of changes in crystallite sizes due to aging. The inset shows a higher-magnification view of the Pt(111) reflection; the size of the peak corresponds to the amount of crystalline Pt in the sample.
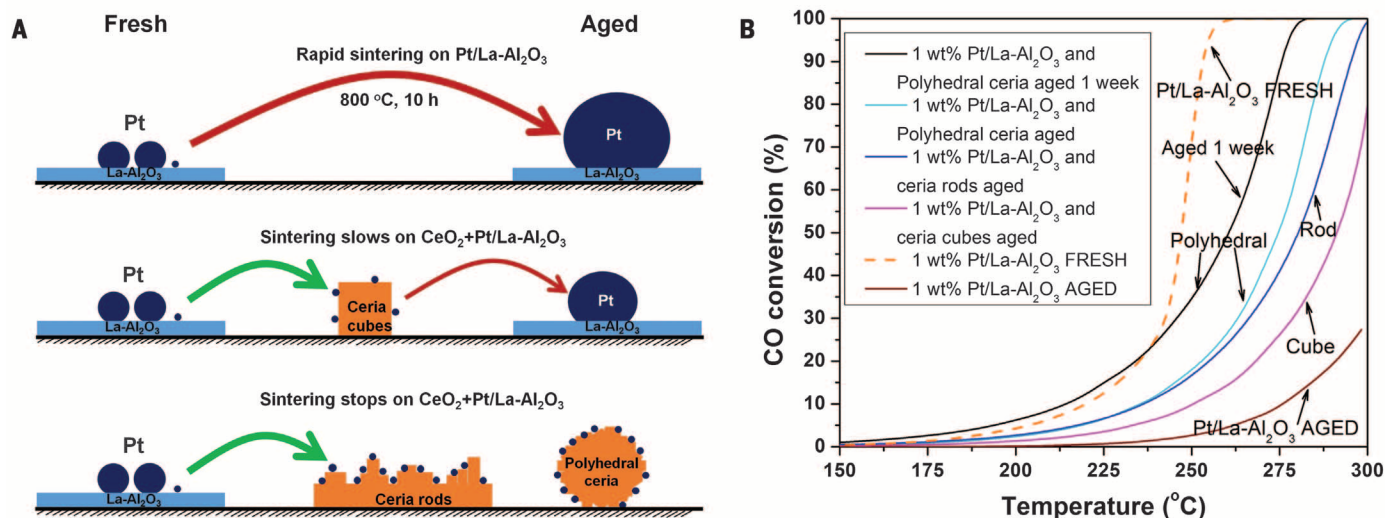
Fig. 2. Physically mixing ceria with Pt/La-Al₂O₃ leads to enhanced reactivity. (**A**) Illustration of Pt nanoparticle sintering, showing how ceria can trap the mobile Pt to suppress sintering. Cubes appear to be less effective than rods or polyhedral ceria. (**B**) Light-off curves for CO oxidation on the 1 wt % Pt/La-Al₂O₃ sample (20 mg of catalyst in the reactor) and the samples physically mixed with ceria (20 mg of 1 wt % Pt/La-Al₂O₃ mixed with 10 mg of ceria powder) and then aged at 800°C in air. The higher reactivity of the samples containing ceria correlates with the smaller Pt peak in the XRD patterns (inset in Fig. 1).

Fig. 3. Heating in air at 800°C allows mobile Pt species to be trapped on ceria. (**A** to **D**) Representative AC-STEM images of 1 wt % Pt/CeO₂-rod [(A) and (B)] and 1 wt % Pt/CeO₂-polyhedra [(C) and (D)] after aging at 800°C for 10 hours in flowing air. The darker objects within the ceria particles are internal voids. The bright dots on the surface of CeO₂ represent mononuclear Pt species that are stable to treatment in flowing air at 800°C. When the ceria lattice is aligned with the electron beam [(B) and (D)], it is more difficult to distinguish the Pt because of the strong contrast from the ceria. The Pt species reside on the surface of ceria rather than being embedded within it.
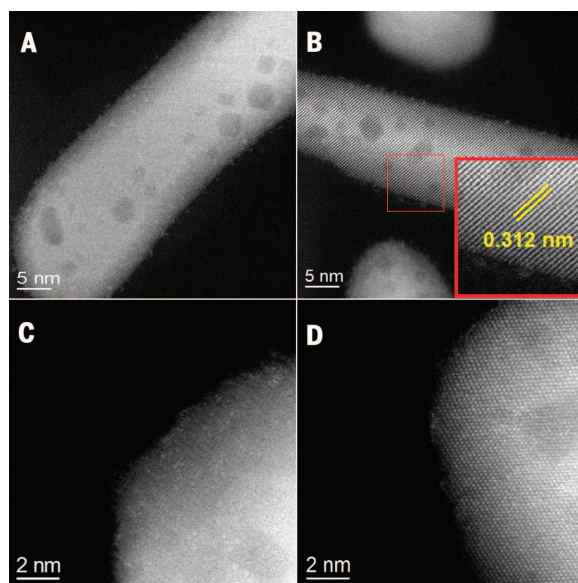

Figure 2A provides a schematic illustration of how physically mixed ceria traps Pt emitted from the alumina catalyst, thereby helping to improve the reactivity for CO oxidation (Fig. 2B). The smaller the Pt peak in the inset in Fig. 1D, the more atomically dispersed Pt that is present on the sample, which leads to higher catalytic activity. The aged Pt/La-alumina had such large Pt crystallites that there was negligible CO oxidation reactivity at 225°C. Among the nanoshapes, the physically mixed polyhedral ceria and the nanorods show similar performance, with the lowest reactivity seen with the ceria cubes. When the physically mixed polyhedral ceria was aged for 1 week with the Pt/La-Al₂O₃, the reactivity was comparable to that of the fresh catalyst (per

gram of catalyst), indicating remarkable sinter resistance (Fig. 2B).

On the basis of the CO oxidation activity shown in Fig. 2, we calculated the specific reactivity [turnover frequency (TOF)] for the Pt (table S2 and fig. S6). Chemisorption of H₂, O₂, and CO was performed on these catalysts (24) after oxidative pretreatments similar to those used for the reactivity measurements. No H₂ or O₂ uptake was detected; the ratio of chemisorbed CO/Pt was 0.18. The low CO uptake would suggest a particle size of ~5 nm, but high-angle annular dark-field (HAADF) AC-STEM imaging showed only atomically dispersed Pt species on the polyhedral ceria and on the ceria rod samples (Fig. 3). The ceria underwent sintering after being heated

at 800°C in air, as seen from the peak widths of the ceria XRD peaks highlighted with asterisks in Fig. 1D. As a result, the rods and cubes changed shape and became more rounded (Fig. 3 and fig. S7). The effect of high-temperature treatment was most severe on the ceria cubes, as seen from the Kα1-Kα2 splitting of the high-angle ceria XRD reflections (Fig. 1D, curve a) indicating large crystallite sizes. We could not image any single-atom Pt species on the ceria cubes; hence, the concentration of atomically dispersed Pt on the cubes is apparently much lower (fig. S7).

Because chemisorption of CO was not useful for counting the number of Pt sites, we used the amount of atomically dispersed Pt derived from the XRD measurements (24). The TOF derived in this manner is remarkably similar for all of these catalysts, within experimental error (0.12 ± 0.04 s⁻¹ at 225°C). Surprisingly, the TOF is also close to that reported for single crystals of Pt(100) (25) at this temperature (0.12 s⁻¹), even though the atomically dispersed Pt is very different from a monolithic single crystal in morphology and nearest neighbors. These TOF values are lower than those reported on the most active Pt/CeO₂ catalysts (26, 27), but the latter contain metallic Pt nanoparticles while our catalysts contain atomically dispersed Pt that is present in ionic form, most likely Pt²⁺. A reaction mechanism based on DFT calculations was proposed for single isolated Pt²⁺ on alumina, and although the mechanism differs from that on metallic Pt, the TOF for CO oxidation was comparable to that on 1 wt % Pt/alumina (28).

Because Pt was deposited through the vapor phase in physically mixed ceria samples, we prepared a second set of catalysts directly on the same ceria powders using a conventional method, impregnation of chloroplatinic acid. These 1 wt % Pt/ceria samples were then aged at similar
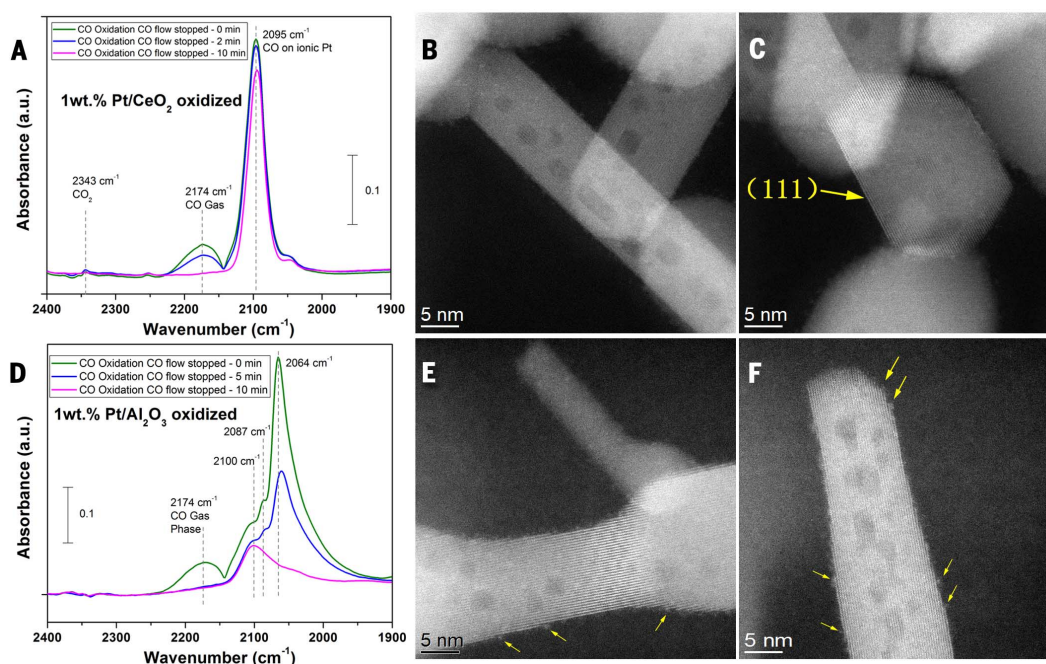
Fig. 4. The atomic dispersion of Pt is preserved during CO oxidation measurements. (**A**) DRIFTS of the 1 wt % Pt/CeO$_2$ polyhedra during CO oxidation at 125°C after oxidative pretreatment in 10% O$_2$ at 450°C. After 30 min of CO oxidation, the CO flow was stopped and spectra recorded at 0, 2, and 10 min while the oxygen flow continued. There is negligible drop in the symmetrical feature at 2095 cm^{-1} that is assigned to isolated ionic Pt sites on the ceria. (**B**, **C**, **E**, and **F**) HAADF AC-STEM images of Pt/ceria rods treated at 800°C in flowing air for 10 hours, before [(B) and (C)] and after three cycles of CO oxidation [(E) and (F)] to 300°C, showing that the catalyst is stable after reaction and the Pt species remain atomically dispersed. The arrows point to step edges that appear to be sites where the Pt species are present, rather than the smooth well-defined (111) facets. (**D**) DRIFTS of a 1 wt % Pt/Al$_2$O$_3$ catalyst after similar pretreatment as in (A) and after 30 min of CO oxidation at 125°C. Spectra were recorded after CO was switched off while the oxygen continued to flow for 0, 5, and 10 min. The band of CO on metallic Pt (2087 cm^{-1} and 2064 cm^{-1}) disappeared rapidly, leaving behind a feature at ~2100 cm^{-1} that corresponds to oxidized Pt.

conditions (800°C in air for 10 hours). The XRD patterns of these aged Pt/ceria samples (fig. S8) show that a well-defined Pt(111) reflection is seen only on the Pt/ceria cube sample, but no Pt(111) reflection is seen on the nanorods or the polyhedral ceria. SEM images (fig. S9) show large Pt particles on the cube sample, but no such large particles were detected on the rod or polyhedral ceria samples. The conversion of CO was marginally higher on the rod samples than on the polyhedral ceria; the cubes were less reactive (fig. S10). TEM images of the Pt species in the physically mixed ceria after aging (fig. S3) are similar to the Pt/ceria prepared by impregnation (fig. S11). The method of Pt deposition does not seem to matter as long as the sample is aged at elevated temperatures in air. The similarity in TOF for Pt/alumina and Pt/ceria suggests that the Pt is not lost into the bulk of the ceria. Solid-solution substitution of platinum for cerium in bulk ceria is unfavorable, given the smaller ionic radii of Pt^{2+} or Pt^{4+}. Platinum cations prefer six-fold octahedral coordination with surrounding oxygens, in contrast to the eight-fold cube coordination of oxygens surrounding cerium cations in CeO$_2$.

We examined the Pt/ceria rod samples after three cycles of CO oxidation going up to 300°C. The Pt was atomically dispersed before (Fig. 4, B and C) and after reaction (Fig. 4, E and F). To examine the nature of the Pt during reaction, we performed DRIFTS of the 1 wt % Pt/polyhedral

CeO$_2$ sample (Fig. 4A) and compared the results with a 1 wt % Pt/Al$_2$O$_3$ sample (Fig. 4D). Both samples were subjected to an oxidative treatment (10% O$_2$ in He at 450°C) before exposure to reaction conditions at 125°C (CO:O$_2$ = 1.5:1). A prominent symmetrical band at 2095 cm^{-1} was the only feature seen on the Pt/CeO$_2$ support (Fig. 4A), whereas on Pt/alumina we observed multiple CO adsorption features typical of metallic Pt nanoparticles, including a band on ionic Pt at ~2100 cm^{-1} (which is seen most clearly when the CO is switched off while oxygen continues to flow for 10 min) (Fig. 4D). The coexistence of Pt ionic species and Pt nanoparticles on alumina and other oxide supports was also noted by Ding *et al.* (*29*). To prepare a sample that contained exclusively ionic Pt (and showing a CO adsorption band similar to Fig. 4A), they used a ZSM-5 support and low metal loading (0.5 wt %). The Pt/ZSM-5 was not stable beyond 1 min during electron microscope imaging, forming Pt nanoparticles (*29*). As seen from the images in Figs. 3 and 4 (*24*), the Pt/ceria is stable in the TEM and during repeated CO oxidation tests. The 2095 cm^{-1} band is the only feature seen even at 350°C during CO oxidation (fig. S12), indicating that Pt nanoparticles do not form under these conditions. As reported by Ding *et al.* (*29*), CO on ionic Pt (2095 cm^{-1}) is not reactive at low temperatures (Fig. 4A), whereas CO on metallic Pt (2064 cm^{-1}) reacts readily with flowing oxygen (Fig. 4D). Despite the transient activity

seen on metallic Pt nanoparticles, both of these catalysts exhibit very low steady-state activity at this temperature (Fig. 2 and figs. S13 and S14) due to strongly bound CO. It is only at higher temperatures that the Pt nanoparticles on alumina and the single-atom Pt on ceria become active (Fig. 2) and exhibit similar specific activity for CO oxidation (table S2).

While ceria helps to trap atomically dispersed Pt, the strong interaction between Pt and ceria also helps preserve the surface area of polyhedral ceria (table S3). We estimate a surface atom concentration of 1.1 Pt atoms/nm^2 in the aged sample (table S3). A recent study (*30*) suggests that step edges on the ceria (111) surface provide stable sites for Pt^{2+}. By engineering the density of surface steps, 80% of the Pt loading of 0.18 monolayer (1 monolayer = 7.9 atoms/nm^2) could be stabilized in the form of Pt^{2+}. This corresponds to 1.2 atoms/nm^2, which is similar to the loading of atomically dispersed Pt that we observed. The high step density was achieved by Dvořák *et al.* (*30*) through deposition of ceria on their CeO$_2$ (111) thin films or via heat treatment. The AC-STEM images, especially those in Fig. 4, suggest that the Pt occupies step edges (arrowed) on the ceria rod sample. On the other hand, the well-defined (111) facet in Fig. 4C does not show any Pt species. DFT calculations suggest that the binding energy of Pt to surface steps on CeO$_2$ (*30*) exceeds that of Pt on CeO$_2$ (111) and also the cohesive energy of bulk Pt. The images in

Figs. 3 and 4 show Pt species located randomly on the ceria surfaces (not embedded in the ceria), with no preference for specific facets.

Atom trapping should be broadly applicable as a method for preparing single-atom catalysts. The approach requires a supply of mobile atoms and a support that can bind the mobile species. Conditions that are conducive to Ostwald ripening, which normally is implicated in the degradation of catalysts (3), are ideal because mobile species are continually being generated. In our work, at the aging temperature of 800°C in air, mobile PtO_2 is rapidly emitted; the estimated lifetime is only a few seconds for a 5-nm Pt crystallite (24). Surface species such as hydroxyls and carbonates, which could prevent the trapping of mobile species, would have desorbed at high temperatures, providing a clean surface for the formation of covalent metal oxide bonds that are needed to stabilize single atoms. Trapping of atoms provides a plausible explanation for the role of ceria in slowing the rates of Ostwald ripening and may help to explain how other supports modify the rates of catalyst sintering.

REFERENCES AND NOTES

1. G. W. Graham et al., Catal. Lett. 116, 1–8 (2007).
2. M. H. Wiebenga et al., Catal. Today 184, 197–204 (2012).
3. T. W. Hansen, A. T. Delariva, S. R. Challa, A. K. Datye, Acc. Chem. Res. 46, 1720–1730 (2013).
4. T. R. Johns et al., J. Catal. 328, 151–164 (2015).
5. J. A. Kurzman, L. M. Misch, R. Seshadri, Dalton Trans. 42, 14653–14667 (2013).
6. C. B. Alcock, G. W. Hooper, Proc. R. Soc. London Ser. A 254, 551–561 (1960).
7. G. Cavataio et al., SAE Int. J. Fuels Lubr. 2, 204–216 (2009).
8. Y.-F. Yu-Yao, J. T. Kummer, J. Catal. 106, 307–312 (1987).
9. J. G. McCarty, K.-H. Lau, D. L. Hildenbrand, Stud. Surf. Sci. Catal. 111, 601–607 (1997).
10. C. Carrillo et al., J. Phys. Chem. Lett. 5, 2089–2093 (2014).
11. G. B. McVicker, R. L. Garten, R. T. K. Baker, J. Catal. 54, 129–142 (1978).
12. Y. Nagai et al., J. Catal. 242, 103–109 (2006).
13. J. A. Farmer, C. T. Campbell, Science 329, 933–936 (2010).
14. J. H. Kwak et al., Science 325, 1670–1673 (2009).
15. B. Qiao et al., Nat. Chem. 3, 634–641 (2011).
16. W.-Z. Li et al., Nat. Commun. 4, 2481 (2013).
17. T. R. Johns et al., ChemCatChem 5, 2636–2645 (2013).
18. H.-X. Mai et al., J. Phys. Chem. B 109, 24380–24385 (2005).
19. S. Agarwal et al., ChemSusChem 6, 1898–1906 (2013).
20. T. Wu et al., J. Phys. Chem. Lett. 5, 2479–2483 (2014).
21. A. Bruix et al., Angew. Chem. Int. Ed. 53, 10525–10530 (2014).
22. A. Neitzel et al., J. Phys. Chem. C 120, 9852–9862 (2016).
23. Z. L. Wang, X. Feng, J. Phys. Chem. B 107, 13563–13566 (2003).
24. See supplementary materials on Science Online.
25. P. J. Berlowitz, C. H. F. Peden, D. W. Goodman, J. Phys. Chem. 92, 5213–5221 (1988).
26. R. Kopelent et al., Angew. Chem. Int. Ed. 54, 8728–8731 (2015).
27. M. Cargnello et al., Science 341, 771–773 (2013).
28. M. Moses-DeBusk et al., J. Am. Chem. Soc. 135, 12634–12645 (2013).
29. K. Ding et al., Science 350, 189–192 (2015).
30. F. Dvořák et al., Nat. Commun. 7, 10801 (2016).

ANIMAL ROBOTICS

Tail use improves performance on soft substrates in models of early vertebrate land locomotors

Benjamin McInroe,[1]* Henry C. Astley,[1]* Chaohui Gong,[2] Sandy M. Kawano,[3] Perrin E. Schiebel,[1] Jennifer M. Rieser,[1] Howie Choset,[2] Richard W. Blob,[4] Daniel I. Goldman[1,5]†

In the evolutionary transition from an aquatic to a terrestrial environment, early tetrapods faced the challenges of terrestrial locomotion on flowable substrates, such as sand and mud of variable stiffness and incline. The morphology and range of motion of appendages can be revealed in fossils; however, biological and robophysical studies of modern taxa have shown that movement on such substrates can be sensitive to small changes in appendage use. Using a biological model (the mudskipper), a physical robot model, granular drag measurements, and theoretical tools from geometric mechanics, we demonstrate how tail use can improve robustness to variable limb use and substrate conditions. We hypothesize that properly coordinated tail movements could have provided a substantial benefit for the earliest vertebrates to move on land.

During the vertebrate invasion of land, 385 to 360 million years ago, early tetrapods and relatives faced a variety of challenges (1), including locomotion in terrestrial environments. Terrestrial locomotion relies on interactions between the body and substrate to generate propulsive forces, but the interaction between the organism and some substrates may be complex. Fossil evidence indicates that tetrapods emerged from water in near-shore habitats, where they likely encountered flowable soft substrates such as sands and muds (2, 3). These substrates exhibit properties of solids and fluids, either jamming or yielding (plastic deformation of the material) depending on how they are loaded (4) and sloped (5).

The challenge of movement on flowable substrates therefore arises from the complexity of interactions between the substrate and the organism. Even on level deformable substrates, subtle variations in limb morphology (6) and kinematics (7) can lead to substantial differences in performance. Furthermore, interactions between appendages and these substrates leave local disturbances, which can influence subsequent interactions, sometimes leading to deteriorating locomotor performance and eventual total locomotor failure (8). As substrate slope increases, yield forces decrease and downhill material flow becomes important, reducing the range of effective locomotor strategies (5).

The use of an additional locomotor structure that can be independently coordinated may allow a greater range of effective behaviors, even in the absence of derived limb morphology and sophisticated motor patterns. We propose that the tail could have been a critical locomotor structure for early tetrapods. In addition to being a primary driver of aquatic locomotion, tails play major roles in the propulsion of many modern fishes during terrestrial locomotion (9–12) and can be used as inertial reorientation appendages in some tetrapods (13, 14). Thus, the use of a prominent tail [as seen in fossil taxa (15–17) (Fig. 1A)] may have increased locomotor robustness to environmental and kinematic variables.

Evaluating locomotor performance for extinct taxa is challenging (18, 19), in part because the sensitivity of locomotion on complex substrates to kinematics and control strategies cannot necessarily be inferred from range of motion and morphology (7). Therefore, to test our hypothesis, we used three complementary modeling methods (Fig. 1): a model organism, a robophysical model, and a mathematical model. We made several choices governing our modeling approaches. In our locomotors, we modeled symmetrical, forelimb-driven

[1]School of Physics, Georgia Institute of Technology, Atlanta, GA, USA. [2]Robotics Institute, Carnegie Mellon University, Pittsburgh, PA, USA. [3]National Institute for Mathematical and Biological Synthesis, University of Tennessee, Knoxville, TN, USA. [4]Department of Biological Sciences, Clemson University, Clemson, SC, USA. [5]School of Biology, Georgia Institute of Technology, Atlanta, GA, USA.
*These authors contributed equally to this work. †Corresponding author. Email: daniel.goldman@physics.gatech.edu

Editor's Summary

Hot single-atom catalysts

For heterogeneous catalysts made from precious metal nanoparticles adsorbed on metal oxides, high temperatures are the enemy. The metal atoms become mobile and the small particles grow larger, causing a loss in surface area and hence in activity. Jones *et al.* turned this process to their advantage and used these mobile species to create single-atom platinum catalysts. The platinum on alumina supported transfers in air at 800°C to ceria supports to form highly active catalysts with isolated metal cations.

Science, this issue p. 150

Article Tools	Visit the online version of this article to access the personalization and article tools: http://science.sciencemag.org/content/353/6295/150
Permissions	Obtain information about reproducing this article: http://www.sciencemag.org/about/permissions.dtl